An optimized full-configuration-interaction nuclear orbital approach to a "hard-core" interaction problem: Application to $(^3He)_N$–$Cl_2(B)$ clusters ($N \leq 4$)

M. P. de Lara-Castells,[1,a] P. Villarreal,[1] G. Delgado-Barrio,[1] and A. O. Mitrushchenkov[2]
[1]*Instituto de Física Fundamental (CSIC), Serrano 123, Madrid E-28006, Spain*
[2]*Laboratoire Modélisation et Simulation Multi Echelle, Université Paris-Est, MSME FRE3160 CNRS, 5 bd Descartes, Marne-la-Vallée 77454, France*

(Received 31 July 2009; accepted 21 October 2009; published online 16 November 2009)

An efficient full-configuration-interaction nuclear orbital treatment has been recently developed as a benchmark quantum-chemistry-like method to calculate ground and excited "solvent" energies and wave functions in small doped ΔE_{est} clusters ($N \leq 4$) [M. P. de Lara-Castells, G. Delgado-Barrio, P. Villarreal, and A. O. Mitrushchenkov, J. Chem. Phys. **125**, 221101 (2006)]. Additional methodological and computational details of the implementation, which uses an iterative Jacobi–Davidson diagonalization algorithm to properly address the inherent "hard-core" He–He interaction problem, are described here. The convergence of total energies, average pair He–He interaction energies, and relevant one- and two-body properties upon increasing the angular part of the one-particle basis set (expanded in spherical harmonics) has been analyzed, considering Cl_2 as the dopant and a semiempirical model (T-shaped) He–$Cl_2(B)$ potential. Converged results are used to analyze global energetic and structural aspects as well as the configuration makeup of the wave functions, associated with the ground and low-lying "solvent" excited states. Our study reveals that besides the fermionic nature of ^{3}He atoms, key roles in determining total binding energies and wave-function structures are played by the strong repulsive core of the He–He potential as well as its very weak attractive region, the most stable arrangement somehow departing from the one of N He atoms equally spaced on equatorial "ring" around the dopant. The present results for $N=4$ fermions indicates the structural "pairing" of two ^{3}He atoms at opposite sides on a broad "belt" around the dopant, executing a sort of asymmetric umbrella motion. This pairing is a compromise between maximizing the ^{3}He–^{3}He and the He-dopant attractions, and suppressing at the same time the "hard-core" repulsion. Although the He–He attractive interaction is rather weak, its contribution to the total energy is found to scale as a power of three and it thus increasingly affects the pair density distributions as the cluster grows in size. © *2009 American Institute of Physics*. [doi:10.1063/1.3263016]

I. INTRODUCTION

Spectroscopic experiments at very low temperatures involving molecules inside helium nanodroplets, since the pioneering studies in 1992,[1] revealed a number of novel features deriving from the quantum nature of this solvent.[2] The paradigmatic infrared spectra of the carbonyl sulfide molecule as a dopant, which depend on the isotope considered, ^{3}He or ^{4}He, represent one of the experimentally most well-documented evidences of the unique properties of He nanodroplets.[3,4] Further, numerous high-resolution spectroscopic studies of different molecules in small doped ^{4}He clusters have been performed in order to analyze how many atoms are required for the onset of superfluid behavior in a microscopic system, and to understand the microscopic mechanisms that govern the transition from van der Waals molecular complexes to quantum solvation.[5–9] It has also given rise to renewed impetus for theoretical studies in which, due to the nonclassical nature of the particles involved, the use of quantum treatments is crucial (see Ref. 10 for a recent review). Zero temperature quantum, both variational and diffusion, Monte Carlo[11–14] and finite temperature path-integral Monte Carlo methods[12,15–17] have been proved to be efficient approaches in describing ground-state energies and structural properties of dopant molecules in ^{4}He clusters. Recently, these methods have been extended to provide imaginary-time correlation functions from which the lowest dopant rotational excitation energies can be extracted.[13,17–19] Theoretical simulations facilitated the interpretation of the evolution of high-resolution spectra of ^4He_N-molecule clusters with N as an indicator of transition from a molecular complex to a quantum solvated system already for $N=4$ (see, e.g., Ref. 9). These interpretations could be assisted by the interplay between experimental and theoretical spectroscopic investigations on small ^3He_N-molecule clusters. However, the status of the techniques to study ^{3}He-molecule clusters is far behind as compared to ^{4}He. An upper bound to the ground-state energy of fermionic ^{3}He clusters is obtained by the fixed-node diffusion Monte Carlo approximation,[11,20]

[a]Author to whom correspondence should be addressed. Electronic mail: delara@imaff.cfmac.csic.es.

which imposes the nodes of a known antisymmetric trial function on the unknown exact wave function. Using the released-node technique, an estimation of the bias introduced by the fixed-node approximation can be obtained.[21]

As an alternative, wave-function-based quantum-chemistry (QC)-like approaches, which consider the ^{3}He atoms as "fermions" (i.e., pseudoelectrons) and the dopant molecule as "pseudonuclei," and replace electron-electron and electron-nucleus Coulomb interactions by He–He and He-dopant pair potentials, was proposed by Jungwirth and Krylov[22] in 2001, and applied to the study of the $(^3\mathrm{He})_2-\mathrm{SF}_6$ trimer. It is worth mentioning that the main approximation in QC-like treatments (i.e., the decoupling of the dopant rotation along with the adiabatic approach for the diatomic stretch) has been recently assessed for heavy as well as light dopant molecules.[23–25] One appealing advantage of the QC-like approaches is that they allow a balanced treatment of doped ^{3}He, ^{4}He, and mixed ^{3}He/^{4}He clusters. Moreover, since the wave function is provided, they allow for spectral simulations and, therefore, proper comparisons with the experiment. Within this framework, Hartree–Fock/Hartree (HF/H) methods have been implemented[26–30] for simulating Raman and infrared spectra of diatomic molecules in fermionic/bosonic He environments.

The main difficulty in developing the QC treatments is caused by the very repulsive He–He short distance interaction (the commonly known "hard-core" interaction problem). Hence, truncated He–He potentials are employed, for example, in density-functional-theory approaches (see, for example, Ref. 10) and HF/H implementations.[26–28] A truncated He–He potential at high energy values was also employed in a recent configuration-interaction treatment by Felker,[31] and applied to the calculation of $J=0$ states in $(^4\mathrm{He})_N-\mathrm{Br}_2$ ($N=1-5$) clusters. As a benchmark method, we recently optimized a nuclear orbital full-configuration-interaction (FCI) treatment[32] to hard-core interaction problems by replacing the commonly used iterative Davidson algorithm of diagonalization[33] by a Jacobi–Davidson (JD) one.[34] In fact, our preliminary application of the method to $(^3\mathrm{He})_N$-diatomic ($N\leq 4$) clusters[32,35] clearly showed the high efficiency of the JD procedure as compared to the standard Davidson algorithm. Also, in agreement with previous Hartree–Fock results,[23,26,27,30] we found a high degree of degeneracy for the lowest-energy spin states. It is worth mentioning that along with the corresponding selection rules this high degeneracy was found to be the principal cause[26] of the broad unstructured spectra exhibited by molecules inside fermionic nanodroplets.[3]

The objectives of this paper are fourfold: (1) to provide the details of our current implementation of the FCI nuclear orbital treatment, (2) to analyze the convergence trends of single- and two-particle properties upon expanding the angular part of the one-particle basis set, (3) to examine converged results in terms of global energetic and structural aspects of small doped ^{3}He clusters in either ground or low-lying excited intermolecular states, and (4) to study the configuration makeup of FCI wave functions, testing simple models to get further insight and to provide hints in devising an optimized approach to handle larger cluster sizes. For this purpose we have chosen to study small $(^3\mathrm{He})_N-\mathrm{Cl}_2(B)$ clusters ($N\leq 4$). Sands *et al.*[36] reported pioneering detailed rotationally resolved spectra of $(^4\mathrm{He})_N-\mathrm{Cl}_2$ ($N=1,2$) for the $B\leftarrow X$ transition and stimulated sophisticated theoretical studies.[37–39] Full dimensional variational calculations at zero total angular momentum, $J=0$, on $(^4\mathrm{He})_2-\mathrm{Cl}_2(B)$ complexes were first realized by Villarreal *et al.*,[37] whereas the study by Hernández *et al.*[38] was first to reveal the importance of considering the ^{4}He permutation symmetry in order to properly simulate the $B\leftarrow X$ spectra. Several Monte Carlo-based studies on $(^4\mathrm{He})_N-\mathrm{Cl}_2(B)$ clusters with $N\geq 2$ have been reported as well.[40–42] Thus, Bačić *et al.*[43] calculated ground-state energies and structures for $N=1-3$, pointing out that these clusters are extremely floppy and that, due to the anisotropy of the $\mathrm{He}-\mathrm{Cl}_2(B)$ interaction, He atoms tend to be localized on a ring perpendicular to the Cl_2 internuclear axis. They also reproduced to better than a 1% the ground state of these clusters as the sum of independent N (lowest-state) $^4\mathrm{He}-\mathrm{Cl}_2$ triatomics and $N-1$ $^4\mathrm{He}_2$ oscillators. Further studies[42] for $N=1-10$ indicated that the He atoms arrange in equivalent positions on the ring around the molecular dopant. More recent calculations[41] for $10\leq N\leq 100$ provided further support for the central-ring structure and indicated the formation of five rings for larger cluster sizes. No previous theoretical studies, however, have been performed on $(^3\mathrm{He})_N-\mathrm{Cl}_2$ clusters taking into account the fermionic nature of ^{3}He atoms.

In the following section, the methodological FCI approach is outlined. Next, details of the calculations are provided in Sec. III. In Sec. IV, one- and two-particles properties of $(^3\mathrm{He})_N-\mathrm{Cl}_2(B)$ clusters in the ground and low-lying excited states are presented and discussed. The discussion is first focused on a convergence analysis with the basis set size and, second, on the behavior of converged energies and natural orbitals (NOs) as the cluster grows in size. Then, one- and two-body spatial density distributions are analyzed and most probable arrangements of the helium atoms around the dopant are suggested. Further, global aspects of FCI wave-functions structures are provided, and finally, we conclude with a summary of the main results and plans for future work. Some additional technical and methodological details of the FCI implementation are described in Appendices.

II. OUTLINE OF THE METHODOLOGICAL APPROACH

A. Quantum-chemistry-like treatment

The details of the present approach to describe a AB diatomic molecule solvated by N ^{3}He atoms have been provided previously.[26,32] In what follows we will only outline the most relevant aspects. As in electronic structure problems, choosing a body-fixed coordinate system with the Z axis parallel to the internuclear diatomic axis, we first solve the Schrödinger equation for the N ^{3}He atoms,

$$[H^{(N)}-E^{(N)}_{\Lambda,S}(r)]\Phi^{(N)}_{\Lambda,S}(\{\mathbf{R}_k\};r)=0, \quad (1)$$

at different fixed values of the diatomic bond length, r. $H^{(N)}$ is the analog to the electronic Hamiltonian,

$$H^{(N)} = \sum_{k=1}^{N} (K_k(\mathbf{R_k}) + V_k^{AB\text{-He}}(\mathbf{R_k};r)) + \sum_{k\le l} V_{kl}^{\text{He–He}}(|\mathbf{R}_k - \mathbf{R}_l|) - \frac{\hbar^2}{m_{AB}} \sum_{k<l} \nabla_k \cdot \nabla_l, \quad (2)$$

where $\mathbf{R_k}$ are the vectors from the diatomic center of mass to the different He atoms. $H^{(N)}$ thus comprises one-particle kinetic, K_k, and potential energy terms, $V_k^{\text{AB-He}}$, as well as two-particle potential, $V_{kl}^{\text{He–He}}$, and kinetic energy coupling, $\nabla_k \cdot \nabla_l$, terms. Note that potential three-body and higher order terms are neglected. The validity of this approach has been confirmed by *ab initio* calculations (see, e.g., Ref. 44). The r-dependent eigenvalues and eigenfunctions are labeled according to the projection of the total orbital angular momenta, $\mathbf{L}=\Sigma_N \mathbf{l}_k$, on the molecular axis, Λ, and the total spin angular momentum, S. For a total angular momentum $\mathbf{J}=\mathbf{j}+\mathbf{L}+\mathbf{S}$ ($\mathbf{j}$ being the diatomic angular momentum) with projection onto the BF Z-axis $\Omega=\Lambda+\Sigma$ (Σ being the projection of S on Z), omitting Coriolis couplings, the effective Hamiltonian of the dopant molecule can be written as

$$H_N^{\text{eff}} = -\frac{\hbar^2}{2m}\frac{\partial^2}{\partial r^2} + U(r) + E_{\Gamma,S}^{(N)}(r) + \frac{\hbar^2}{2mr^2}G. \quad (3)$$

Neglecting nonadiabatic corrections and averaging $\mathbf{L}$ over the total helium wave function at $r=r_e$, G is approximated by

$$G \approx J(J+1) + \langle \mathbf{L}^2 \rangle - 2(\Lambda^2 + \Sigma^2 + \Lambda\Sigma). \quad (4)$$

In practice, either $\langle \mathbf{L}^2 \rangle$ values or $P(L)$ distributions[28] [replacing $\langle \mathbf{L}^2 \rangle$ by $\Sigma P(L)L(L+1)$ in Eq. (4)], are used to get G (see Appendices A and B). Since $\langle \mathbf{L}^2 \rangle$ is a two-particle property, we need wave-function-based methods (or methodologies which are able to provide the second-order reduced density matrix). Then the modified Schrödinger equation can be solved to calculate the eigenvalues and spectrum of the distorted dopant molecule as presented elsewhere.[26]

B. Full-configuration-interaction implementation

In order to solve Eq. (1), we implemented an efficient FCI code, which is a modified version of the DYNAMIC CI program.[45] This program uses a N-particle basis set of configuration state functions (CSFs), which are the spin-adapted linear combinations of Slater determinants as described, e.g., in Ref. 46. The CSFs are constructed in the same way as in MOLPRO program package;[47] these are genealogical wave functions, ordered according to inverse lexical order.[48,49]

Slater determinants, in turn, are built using one-particle functions, formed as linear combinations of "atomic" orbitals. In practice, starting with the smallest basis set size, the initial orbitals were derived from the diagonalization of the Hamiltonian corresponding to an independent-particle approximation. Next, we used an increasing-orbital-space technique in which the configuration-interaction (CI) vectors obtained for each cluster size, spacial symmetry, and spin value from the previous calculation with a smaller basis are projected on the expanded one-particle representation space. This, together with restarting iterative CI procedure from the corresponding CI vectors, provided a faster convergence of the whole process. The atomic orbitals used in this work are the products of numerical radial functions and spherical harmonic $Y_{\ell m}$ with all $\ell \le \ell_{\max}$ and $|m| \le \min(\ell, m_{\max})$. The radial functions, F_n ($n=1\cdots n_{\max}$), were constructed by orthogonalization of the lowest-energy solutions from the Schrödinger equation associated with the ^{3}He-AB triatomic at $n_{\max}$ fixed angular orientations of the He atoms with respect to the diatomic, θ_n, as described in detail in Refs. 28 and 37. Explicit integral expressions in this one-particle basis representation have been provided in Ref. 28.

The full-CI program is of an iterative direct-CI type, i.e., it does not use the matrix to diagonalize explicitly, but rather its action on an arbitrary trial vector must be provided. In electronic structure calculations the standard Davidson method[33] is the most commonly used iterative eigensolver, its success being mostly due to the typical strong diagonal dominance of quantum-chemistry Hamiltonians. However, due to the hard-core He–He interaction at short distances, very large off-diagonal Hamiltonian elements appear in our case and the standard Davidson algorithm has very poor convergence properties. In contrast, the JD method[34] with SYMMLQ linear solver[50] have been found to converge much better as compared to the standard Davidson method. This behavior has been already analyzed in detail for clusters containing Br_2 and Cl_2 as dopant species.[32,35]

Since the inclusion of kinetic energy couplings [last term in Eq. (2)] into the two-particle integrals breaks permutational-symmetry properties, these terms were not accounted for during full-CI calculation but they were evaluated afterwards as a perturbative correction,

$$\Delta E_{\text{ck}} = -\frac{\hbar^2}{m_{AB}} \sum_{ijkl} (\nabla)_{ij} \cdot (\nabla)_{kl} \Gamma_{ij;kl}, \quad (5)$$

with Γ being the standard two-particle reduced density matrix. We verified that its contribution to the total energy, owing to the relatively Cl_2 high mass, is very small (less than a 1%) and can be safely neglected. Therefore, the results presented in the following sections do not contain this correction.

III. POTENTIAL ENERGY SURFACES AND NUMERICAL DETAILS

In the calculations presented here a grid of 5000 points in the range [1.5–18.5] Å was employed to get the numerical radial functions. He–Cl_2 and He–He interaction potentials were expanded in a basis of 60 and 300 Legendre polynomials, respectively. We used a basis set comprising spherical harmonics $Y_{\ell m}$ with $6 \le l_{\max} \le 9$ and $3 \le |m_{\max}| \le l_{\max}$, and $n_{\max}=4$ numerical radial functions (i.e., from 148 to 400 orbitals). The set of θ_n values, $\theta_n = \pi/2 - (n-1)\pi/24$ ($n=1,\ldots,n_{\max}$), was chosen to describe properly the neighborhood of the T-shaped equilibrium angular region. This representation basis is further transformed to real spherical harmonics, and the orbitals are classified with respect to the irreducible representations of the D_{2h} point group (the highest symmetry group that can be used in our CI program). With this basis we were able to reliably perform full-CI calculations with up to four fermions, looking for the lowest

eigenvalue associated with each possible total spin value and spatial D_{2h} symmetry. The largest size of the FCI calculations presented here is for the triplet states of $(^3He)_4-Cl_2$ clusters, about 170×10^6 of CSFs. The convergence thresholds for the total energy, $E^{(i)}-E^{(i-1)}$ (i standing for the ith outer JD iteration[32]), was set to 10^{-9} cm^{-1}. With this threshold, the norms of the residual vectors [defined as $|(E-\hat{H})\mathbf{C}|$, $\mathbf{C}$ being the approximation to the eigenvector] were less than 3×10^{-3} cm^{-1} in all cases.

As in previous works,[26–28] the $He-Cl_2(B)$ PES was modeled as a pairwise addition of Morse-type He–Cl pair interactions[43] whereas the He–He interaction was described by the semiempirical Aziz and Slaman's potential,[51] the Cl–Cl bond length being fixed to its equilibrium value (2.41 Å). Presently, there are $He-Cl_2(B)$ potential energy surfaces (PESs) based on either high-level *ab initio* calculations or accurate fits available (see, e.g., Ref. 52). These PESs show very good agreement in the energy (~30 cm^{-1}) and position of the minimum (at a perpendicular configuration) and differ a little in the linear configuration, which is found to be deeper (~5 cm^{-1}) in highly accurate *ab initio* calculations.[53] The used B PES is rather anisotropic with a T-well minimum of about −28 cm^{-1} (R_e =3.38 Å), which gradually decreases up to ~−14.6 cm^{-1} (R_e=4.81 Å) at linear conformations. The energy and position of the potential minimum at these two configurations agree to within 5% with those corresponding to the recent B PES proposed from multiproperty fits by García-Vela.[52] Therefore, the model T-shaped PES is considered good enough as an example of a highly anisotropic He-dopant interaction. A careful comparison with possible spectroscopic experiment measurements on $(^3He)_N-Cl_2$ complexes, however, would require the use of a more accurate potential.

IV. RESULTS AND DISCUSSION

A. Basis set convergence of one- and two-particle properties

1. Basis set convergence: Lowest-energy "cluster" states

a. Convergence of energies In order to analyze the convergence of the FCI results with the basis set size, we first compare in Fig. 1(a) ground state energies of $(^3He)_N-Cl_2(B)$ clusters using different ℓ_{max} and m_{max} values. We stress here that FCI results are already well converged with respect to the total number of radial basis functions, n_{max}. For example, the increase in n_{max} from 4 up to 5 [using basis sets with $\ell_{max}(=m_{max})$ values ranging from 6 to 9], results in the lowering of ground-state energies for N=2 by an almost constant value of −0.02 cm^{-1}. Conversely, one clearly notices a strong dependence of the FCI energies on the m_{max} values in Fig. 1(a). In fact, as already mentioned in Ref. 35, it is apparent from the results for ℓ_{max}=6 and N=4 that quite large m_{max} values (≥4) are necessary to make the cluster bound. This is in contrast with previous studies using a Hartree–Fock approach combined with a truncated He–He potential in which the total energies were already converged for m_{max}=3 (see, e.g., Ref. 26). In fact, the strong dependence of FCI results on m_{max} values is a direct consequence of the hard-core repulsion experienced by He atoms in close spacial regions, this being softened within a Hartree–Fock-type implementation.[23,26,27] Overall, the larger the ℓ_{max} and m_{max} values, the clearer the linear behavior of the energies with N. In view of these results, we can further analyze our previous FCI study of small $(^3He)_N-Br_2$ clusters,[32] where a value m_{max}=3 was used. In particular, we notice a deviation from the rather linear behavior of ground-state energies with N for N=4, similar to m_{max}=4 in $(^3He)_N-Cl_2$ clusters [see Fig. 1(a)]. From the results presented here it is clear that this behavior is a consequence of the incompleteness of the basis set to span the azimuthal region and not of the formation of a subshell for N=3. Apparently in the chlorine case a higher m_{max} value is necessary to make the cluster bound for N=4. However, we mention that the calculations with Br_2 as a dopant were performed with ℓ_{max}=8, while the results in Fig. 1 correspond to ℓ_{max}=6. Note also that basis sets with ℓ_{max} =6 and $m_{max}<\ell_{max}$ incorrectly identify the symmetry and the spin of the ground state for N=4, which is $^3\Sigma_g^-$. For example, for m_{max}=3, the lowest-energy state is assigned to a $^5\Sigma_u^+$ one, while for m_{max}=4 or 5, the $^1\Sigma_g^+$ state has the lowest energy. A better test of basis set convergence properties can be performed by comparing two-particle properties. For this purpose, we first plot the average He–He energy values, $\langle V^{He-He}\rangle$, per He–He pair in Fig. 1(b). Similar to total energies, we can notice that the larger ℓ_{max} and m_{max} values, the clearer the linear behavior of $\langle V^{He-He}\rangle$ with N. Also, a departure from this behavior can be found for N=3 when using small ℓ_{max} and m_{max} values. For $\ell_{max}=m_{max}$=8, $\langle V^{He-He}\rangle$ values have already converged to within 0.05 cm^{-1}.

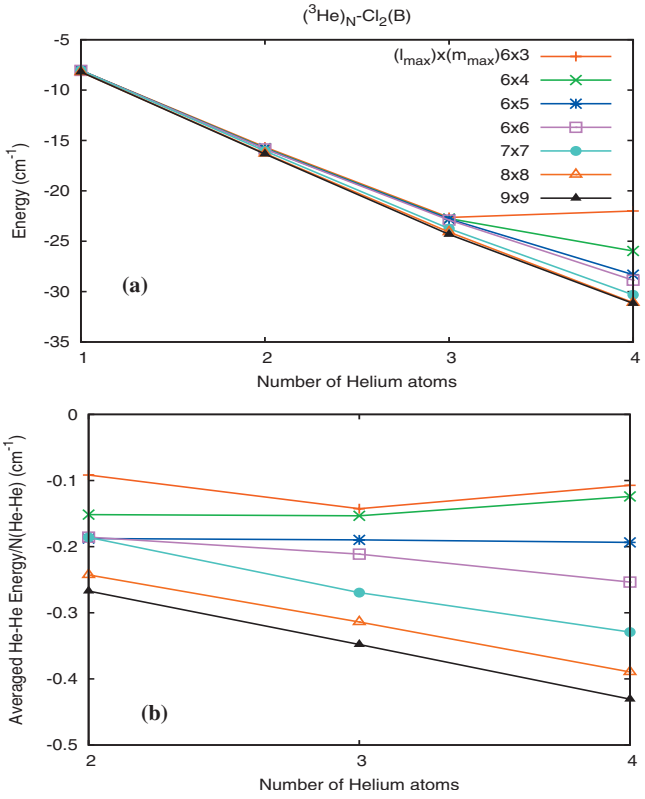

FIG. 1. (a) Ground state total energies (cm^{-1}) of $(^3He)_N-Cl_2(B)$ clusters as a function of the cluster size for different ℓ_{max} and m_{max} values. (b) Average He–He interaction, $\langle V^{He-He}\rangle$ (cm^{-1}), divided by the number of He–He pairs.

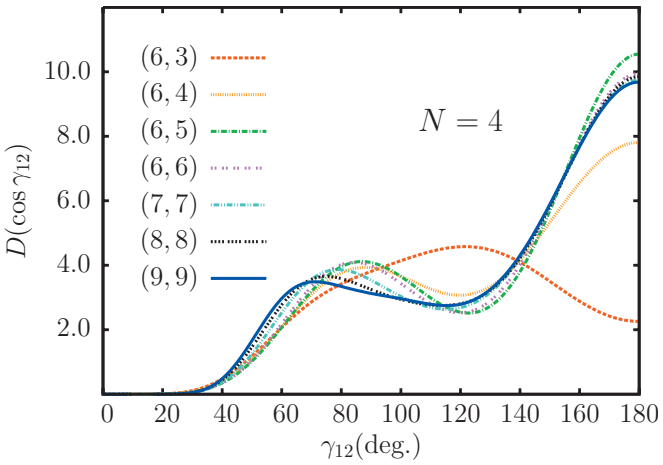

FIG. 2. Two-body density distributions as a function of γ_{12} in the lowest-energy states of $(^3He)_4$–Cl_2 clusters. The probability densities have been calculated with different ℓ_{max} and m_{max} values. The densities are normalized as $\int D(\cos\gamma_{12})d\cos\gamma_{12}=\binom{N}{2}$.

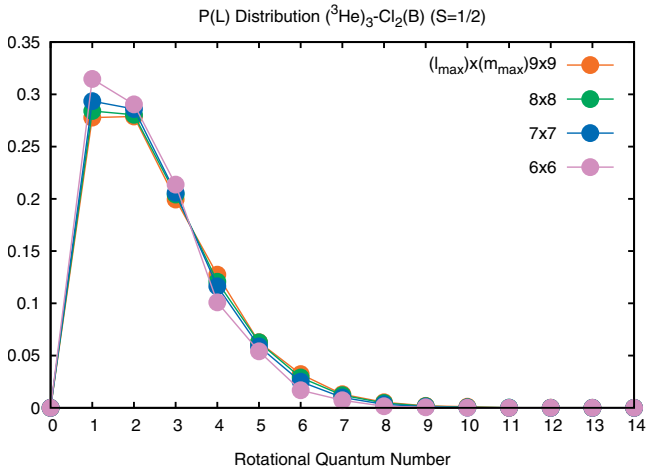

FIG. 3. Total angular momentum distributions, $P(L)$, in the lowest-energy doublet spin-symmetry state of a $(^3He)_3$–$Cl_2(B)$ cluster for different ℓ_{max} ($m_{max}=\ell_{max}$) values.

b. Convergence of pair density distributions In order to analyze convergence properties of eigenfunction, we plotted in Fig. 2 the probability density distributions $D(\cos\gamma_{12})$, where $\cos\gamma_{12}=\mathbf{R}_1\cdot\mathbf{R}_2/R_1R_2$ (i.e., the angle between the position vectors of two helium atoms) for different ℓ_{max} and m_{max} values and $N=4$. The analysis of converged distributions as a function of N will be given in Sec. IV. As a consequence of the "constrained" azimuthal region expanded by the basis set with $m_{max}=3$, the distribution is dramatically different. Much more similar distributions to the converged case are obtained with $m_{max}=4$ and $\ell_{max}=8$; however, only when $m_{max}=\ell_{max}$ similar weights of the peak at 180° are displayed. In general, the smaller the m_{max} and ℓ_{max} values, the faster the decay of the probabilities as γ_{12} approaches to the forbidden region around 0°. For $m_{max}=\ell_{max}$ and $N=4$, note that, as ℓ_{max} increases, the second local maxima are shifted from $\gamma_{12}\sim 90°$ to 70°. Overall, the distributions for $\ell_{max}=m_{max}=8$ can be considered as well converged. In the following we shall therefore continue our analysis using only $m_{max}=l_{max}$ basis sets.

We also analyzed the variation of the total angular momentum, $P(L)$ distribution with ℓ_{max}. We stress here that the basis set convergence of **L**-derived properties is important since, as above mentioned, either $\langle\mathbf{L}^2\rangle$ values or $P(L)$ distributions are used to calculate the spectrum of the distorted dopant molecule. As an illustrative case, the distributions associated with the lowest-energy doublet for $N=3$ (the $^{1/2}\Pi_u$ state) are displayed in Fig. 3. We can see that the distributions are quite similar. In fact, the maximum differences of $P(L)$ values with respect to the $\ell_{max}=9$ case are only of 2.6×10^{-2}, 1.1×10^{-2}, and 6.80×10^{-3} for $\ell_{max}=6$, 7, and 8, respectively.

2. Basis set convergence: Ground and excited cluster states

Table I lists FCI energies of the $(^3He)_N$–$Cl_2(B)$ clusters for different ℓ_{max} values. For $\ell_{max}=9$ and $N=4$, we have not attempted to realize FCI calculation for the singlet and triplet states since the computation (Hamiltonian matrices of $\sim 400\times10^6$ of CFSs) would become too expensive. From Table I one can notice that, regardless of the ℓ_{max} value, symmetries of ground and excited states are the same for any cluster size. By comparing the results for $\ell_{max}=8$ and 9, we can note that, for any symmetry and spin value, total energies converged to within 0.07, 0.18, 0.34, and 0.59 cm^{-1} for $N=1$, 2, 3, and 4, respectively. These values represent less than 2% of the ground-state energies for any N-sized complex. The convergence rate with respect to the ℓ_{max} value depends on the state symmetry and the odd/even character of the added ℓ. In the $N=1$ case, this is clear since the eigenvectors must conserve the parity of ℓ. In this way, g-parity states only contain odd ℓ harmonics and the energies are invariant when an even ℓ value is added to the basis set. The He–He interaction mixes odd and even ℓ orbitals and the convergence rate is increasingly less dependent on the odd/even character of the added ℓ value as N increases. By comparing excitation energies within the (4,2) manifold for $\ell_{max}=8$ and 9, we can note that they converged to within 0.05 cm^{-1} for $\ell_{max}=8$. On the other hand, for any number of particles, the energy differences between the lowest-energy states of each multiplet are less than 0.5 cm^{-1}, showing an overall decrease with the basis set size.

On the whole, FCI eigenvalues and eigenvectors obtained by using the $\ell_{max}=8$ ($m_{max}=\ell_{max}$) basis set can be considered well converged. Below, unless otherwise noted, we shall continue the discussion by focusing on the results obtained with that basis.

B. Analysis of global energetic aspects and natural orbital makeup

1. Global energetic aspects

a. Ground cluster states As above mentioned, converged ground-state total energies show a quasilinear dependence on the number of ^{3}He atoms, as the lowest-state of the triatomic would be occupied by N ^{3}He atoms. As first glance, this is appealing for two reasons. First, we are dealing with a strong correlated system (owing to the hard-core interaction). Second, Fermi–Dirac statistics prevents the same one-

TABLE I. FCI energies (in cm^{-1}) of $(^3He)_N-Cl_2(B)$ clusters using $6 \leq \ell_{max}(=m_{max}) \leq 9$. The states are classified according to the number of fermions (N), the total spin (S), and the symmetry within the D_{2h} point group (the corresponding $D_{\infty h}$ symmetry is indicated in parentheses). Values in boldface correspond to the lowest-energy states within a given (N,S) manifold. The smallest basis-set results ($\ell_{max}=6$) are from Ref. 35.

			$\kappa=+1$			$\kappa=-1$		
N	S	ℓ_{max}	A_g	B_{3u}/B_{2u}	B_{1g}	B_{1u}	B_{2g}/B_{3g}	A_u
1	1/2	6	**−8.05** (σ_g)	−7.43 (π_u)	−6.43 (δ_g)	−3.14 (σ_u)	−2.93 (π_g)	−1.39 (δ_u)
		7	**−8.05**	−7.76	−6.43	−3.45	−2.93	−1.80
		8	**−8.20**	−7.76	−6.63	−3.45	−3.08	−1.80
		9	**−8.20**	−7.83	−6.63	−3.51	−3.08	−1.87
2	0	6	**−15.84**($^1\Sigma_g^+$)	−14.91($^1\Pi_u$)	−14.81($^1\Delta_g$)	−11.02($^1\Sigma_u^+$)	−10.86($^1\Pi_g$)	−10.48($^1\Sigma_u^-$)
		7	**−16.04**	−15.31	−15.34	−11.38	−11.20	−10.87
		8	**−16.29**	−15.50	−15.44	−11.56	−11.36	−11.04
		9	**−16.34**	−15.61	−15.56	−11.63	−11.43	−11.15
	1	6	−14.38($^3\Delta_g$)	**−15.49**($^3\Pi_u$)	−14.87($^3\Sigma_g^-$)	−11.01($^3\Sigma_u^+$)	−10.80($^3\Pi_g$)	−10.26($^3\Sigma_u^-$)
		7	−14.54	**−15.88**	−15.60	−11.40	−11.18	−10.72
		8	−14.94	**−16.07**	−15.69	−11.59	−11.34	−10.94
		9	−15.02	**−16.16**	−15.87	−11.69	−11.43	−11.09
3	1/2	6	−22.45($^2\Delta_g$)	**−22.91**($^2\Pi_u$)	−22.45($^2\Delta_g$)	−18.45($^2\Sigma_u^+$)	−18.29($^2\Pi_g$)	−18.38($^2\Sigma_u^-$)
		7	−23.17	**−23.59**	−23.17	−19.09	−18.95	−19.08
		8	−23.54	**−23.95**	−23.54	−19.49	−19.26	−19.39
		9	−23.74	**−24.15**	−23.74	−19.69	−19.49	−19.58
	3/2	6	−20.63($^4\Delta_g$)	−21.75($^4\Phi_u$)	**−22.90**($^4\Sigma_g^-$)	−17.81($^4\Delta_u$)	−18.18($^4\Pi_g$)	−18.22($^4\Sigma_u^-$)
		7	−21.72	−22.36	**−23.75**	−18.43	−18.98	−18.98
		8	−22.25	−22.86	**−24.09**	−18.88	−19.34	−19.33
		9	−22.59	−23.08	**−24.32**	−19.12	−19.59	−19.56
4	0	6	**−28.74**($^1\Sigma_g^+$)	−25.33($^1\Pi_u$)	−28.42($^1\Delta_g$)	−24.27($^1\Delta_u$)	−24.27($^1\Pi_g$)	−24.91($^1\Sigma_u^-$)
		7	**−30.18**	−27.47	−29.95	−25.58	−25.73	−26.11
		8	**−31.07**	−28.46	−30.66	−26.40	−26.53	−26.73
	1	6	−26.74($^3\Gamma_g$)	−28.61($^3\Pi_u$)	**−28.87**($^3\Sigma_g^-$)	−24.35($^3\Sigma_u^+$)	−24.64($^3\Pi_g$)	−24.38($^3\Sigma_u^-$)
		7	−28.42	−30.07	**−30.32**	−25.68	−25.95	−25.75
		8	−29.33	−30.96	**−31.09**	−26.51	−26.75	−26.61
	2	6	**−28.13**($^5\Delta_g$)	−25.01($^5\Pi_u$)	**−28.13**($^5\Delta_g$)	−23.48($^5\Delta_u$)	−24.15($^5\Pi_g$)	−24.69($^5\Sigma_u^-$)
		7	**−29.59**	−26.77	**−29.59**	−24.86	−25.49	−26.05
		8	**−30.60**	−28.52	**−30.60**	−25.81	−26.41	−26.92
		9	**−31.17**	−29.11	**−31.17**	−26.39	−26.99	−27.44

particle state to be occupied by more than two ^{3}He atoms (Pauli principle). Previous works for the ^{4}He isotope case[37,38,43] also showed that ground-state energies can be very well reproduced by the sum of those for N lowest-state triatomics. However, note that in a bosonic system all particles are allowed to occupy the same one-particle state. Also it is remarkable that, despite the hard-core interaction and the fact that two isolated ^{3}He atoms are not bound (a minimum number of ~30 He atoms is necessary for self-binding[21]), resulting average ^{3}He–^{3}He interaction energies per pair [see Fig. 1(b)] are slightly negative with values oscillating between ~−0.2 and −0.4 cm^{-1} (for $\ell_{max}=8$). Moreover, we tested that the total expectation values $\langle V^{He-He}\rangle$ scale as a power of three with N. Therefore, it appears that the increment in the total energy, owing to the occupation of triatomic excited states, is somewhat compensated by the contribution of $\binom{N}{2}$ effective bound ^{3}He–^{3}He pairs. In this respect, it should be noted that an additive model similar to that proposed by Bačić *et al.*[43] (see Sec. I) could not be applied here, since isolated ^{3}He–^{3}He pairs do not have bound states. A further partition of the one-particle energy into kinetic, $\langle K\rangle$, and He-dopant potential contributions, $\langle V^{He-Cl_2}\rangle$, shows that the expectation values $\langle V^{He-Cl_2}\rangle$ can be approximated to better than a 1% to the one of N triatomics, whereas the values $\langle K\rangle$ overpass those of N triatomics by a magnitude very similar to the total, attractive, He–He contribution.

b. Excited cluster states In what follows, the states that are invariant under reflexion on a mirror plane perpendicular to the dopant molecular axis (z-reflexion) will be marked with $\kappa=1$ whereas those states that are antisymmetric will be denoted with $\kappa=-1$. Apart from the high degree of degeneracy for the lowest-energy spin states (see Table I) already found in previous works,[32,35] it is worth stressing that these states also share very similar kinetic, He-dopant and He-He potential energy contributions. Note also that the energy difference between states with the same spatial symmetry and different spin multiplicities is within only 0.6 cm^{-1} for $\kappa=-1$ eigenfunctions and as large as 2.50 cm^{-1} for $\kappa=+1$ ones. For example, the $^1\Pi_g/^3\Pi_g$ states are degenerated for $N=2$. Due to the T-shaped character of the He–$Cl_2(B)$ PES, the lowest-energy $\kappa=-1$ one-particle state (the $1\sigma_u$ state) has a rather high energy as compared to the ground $1\sigma_g$ ($\kappa=+1$) state. Thus, the promotion energy from the lowest $\kappa=+1$ state to the $\kappa=-1$ state varies from 4.7 cm^{-1} for $N=1$ to 4.2 for $N=2$. Obviously, this picture would be significantly different for a He-dopant potential having minima

TABLE II. NO occupation numbers, τ, greater than 0.005 associated with the lowest-energy states of $(^3\mathrm{He})_N-\mathrm{Cl}_2(B)$ clusters at each (N,S) manifold [using $\ell_{\max}(=m_{\max})=8$]. First column indicates $D_{\infty h}$ symmetries of the NOs (ℓ_z is the orbital angular momentum projection on the Z axis) whereas orbital energies, ϵ, are tabulated in the second column.

		τ (NO occupation numbers) (N,S)						
(ℓ_z)	ϵ (cm^{-1})	(2,0)	(2,1)	(3,1/2)	(3,3/2)	(4,0)	(4,1)	(4,2)
$1\sigma_g(0)$	−8.20	1.54	0.99	1.26	0.98	0.96	1.16	0.96
$1\pi_u(\pm1)$	−7.76	0.39	0.99	1.42	1.90	1.97	1.75	1.83
$1\delta_g(\pm2)$	−6.63	0.06	0.01	0.26	0.04	0.77	0.77	0.96
$1\phi_u(\pm3)$	−4.64			0.04	0.05	0.17	0.22	0.13
$1\gamma_g(\pm4)$	−2.05			0.01	0.02	0.09	0.06	0.08
$1\eta_u(\pm5)$	−0.09					0.02	0.02	0.02

at both T-shaped and linear configurations. Such an analysis is currently in progress.[54] It is also worth mentioning that the total He-dopant potential contribution can be reproduced (within better than a 3%) to the one of N lowest-state triatomics for $\kappa=+1$ and the sum of $N-1$ lowest-state triatomics and one excited triatomic in the $1\sigma_u$ state for $\kappa=-1$ states. The He-dopant interaction is thus maximized independently of the number of particles or state symmetry. Also, the expectation values $\langle V^{\mathrm{He-He}}\rangle$ vary very little (less than 0.7 cm^{-1}).

2. Natural orbitals

Single-particle orbitals diagonalizing the first-order density matrix define the effective nuclear NOs. Table II lists the occupation numbers τ of the relevant NOs for the lowest-energy states of the different (N,S) manifolds. For the sake of simplicity, we have not shown the convergence of τ values upon increasing the basis set size. We only mention that they converged to better than a 10% of the values attained for $\ell_{\max}=9$. Note that irrespective of the cluster size, the sum of τ values listed in Table II represents more than 99.25% of N, while the rest is distributed among remaining NOs, as many as 313. Again, this fact demonstrates the robustness of the nuclear orbital approach for the helium wave function.[32,35] On the other hand, the relative population in the minimal set of NOs is as low as 90%.

Let us now consider how the relevant NOs are populated for ground-state N-sized complexes as N increases. We notice here that the relevant NOs are only slightly different from the $N=1$ independent-particle eigenvectors. As an illustrative example, isoprobability surfaces associated with NOs are shown in Fig. 4 for the ground-state $(^3\mathrm{He})_4-\mathrm{Cl}_2(B)$ complex. We also tabulated in Table II (second column) and Fig. 4 the energies of the independent-particle orbitals correlating with the NOs. These energy levels are roughly rotational energy levels of a rigid rotor on a reduced one dimensional model implying only the azimuthal angle. Within this model, the energy difference between the lowest $1\sigma_g(\ell_z=0)$ and the excited $(\ell_z>0)$ independent-particle states can be approximated by $B_{\mathrm{eff}}m^2$, where B_{eff} ($\sim$0.4 cm^{-1}) is an effective rotational constant whose value is very close to the expectation value $\langle 1/2\mu R^2\rangle$ for the $1\sigma_g$ state. It is worth noting that, although we are dealing with a hard-core interaction problem, the dominant configuration as well as the symmetries of the lowest-energy states FCI wave functions are mainly determined by the energetic spectrum of the $N=1$ independent-particle Hamiltonian and, owing to the fermionic character of the ^{3}He atoms, by the Pauli exclusion principle together with the Hund's rules. For example, the ground and first excited $N=1$ eigenstates are the $1\sigma_g$ ($\epsilon=-8.20$ cm^{-1}) and the $1\pi_u$ ($\epsilon=-7.76$ cm^{-1}) ones, ground-state FCI wave functions for $N=2$ ($^1\Sigma_g^+$) and $N=4$ ($^3\Sigma_g^-$) are dominated by $(1\sigma_g)^2$ and $(1\sigma_g)^2(1\pi_{u,x})(1\pi_{u,y})$ configurations, respectively. Similarly, the FCI wave functions associated with the first excited state for $N=2$ ($^3\Pi_u$) and for $N=4$ ($^1\Sigma_g^+$) are mainly formed by $(1\sigma_g)(1\pi_u)$ and $(1\sigma_g^2)(1\pi_{u,x(y)}^2)$ configurations, respectively. As expected, the lowest-energy highest spin-multiplicity states have the clearest dominant configurations, which is reflected by the highest τ values associated with the minimal set of relevant NOs (equal to N). Even in those cases, however, the τ values of NOs associated with higher m values (see Table II) are not negligible. The high multiconfigurational character of the wave functions for lower spin states is clearly demonstrated by a fact that the occupation numbers of lowest-energy NOs are far from 2. Thus, although the ground state for $N=2$ is dominated by a $(1\sigma_g)^2$ configuration, there are important contributions of virtual excitations from

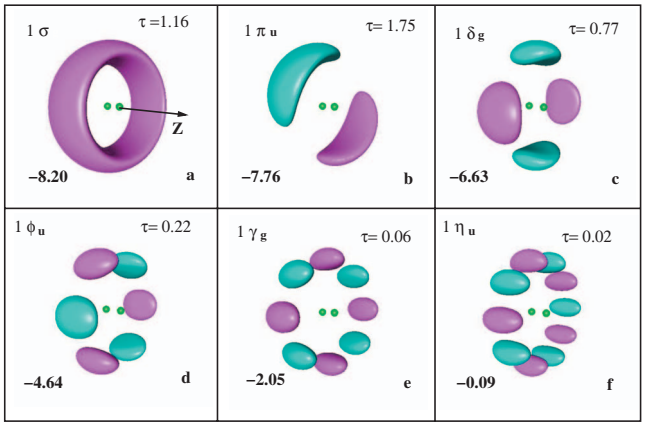

FIG. 4. Representation of relevant NO isoprobability surfaces of the ground state $(^3\mathrm{He})_4-\mathrm{Cl}_2(B)$ complex ($^3\Sigma_u^-$ state) using $\ell_{\max}=8$ ($m_{\max}=\ell_{\max}$). NO occupation numbers, τ, and single-particle energies of the corresponding $N=1$ eigenstates are also shown. The position of the Cl atoms are indicated by small green balls. Purple and green colors indicate positive and negative lobes of the orbitals, respectively. The probability values have been selected to be the half of the maximum value attained at each NO.

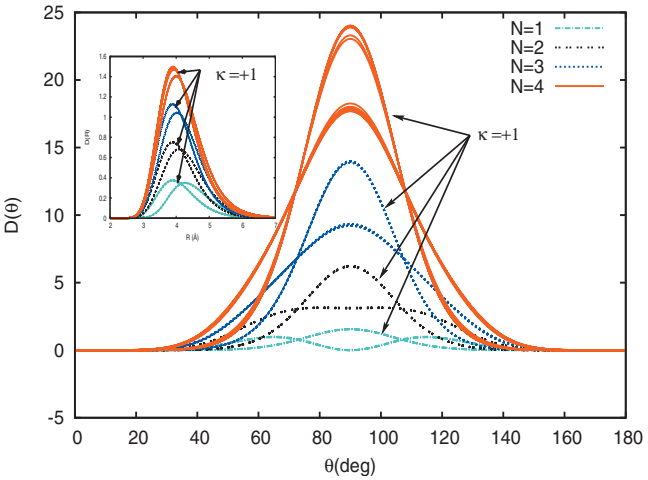

FIG. 5. One-body angular He density distributions of $Cl_2(X)-(^3He)_N$ clusters in their ground and low-lying excited states (from $N=1$ up to $N=4$) using the $\ell_{max}=8$ ($m_{max}=\ell_{max}$) basis set. The densities are normalized as $\int D(\theta)d\theta=N$. Inset: one-body radial density distributions normalized to the number of helium atoms.

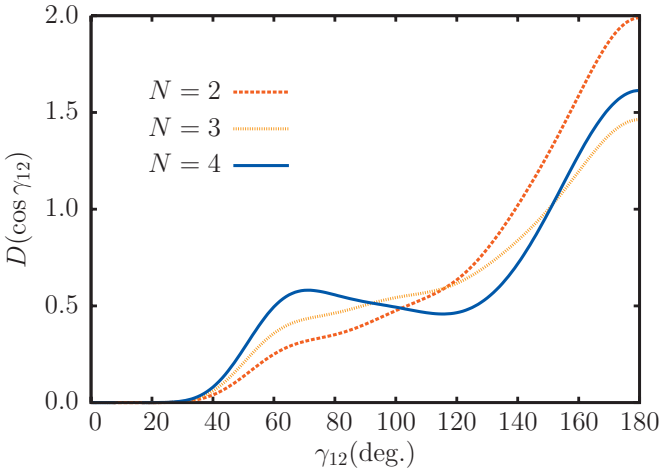

FIG. 6. Angular two-body density distributions, $D(\cos\gamma_{12})$, in the lowest-energy states of $(^3He)_N-Cl_2(B)$ clusters [using $\ell_{max}=8$ ($m_{max}=\ell_{max}$)]. The densities have been renormalized to the unity for all cluster sizes.

the $1\sigma_g$ NO to the $1\pi_u$ and $1\delta_g$ orbitals. Indeed, as the cluster size increases, τ values of the $1\sigma_g$ NO for states comprising $(1\sigma_g)^2$ configurations in the dominant reference state become close to one (see, for example, τ values in Fig. 4).

C. Analysis of one- and two-body density distributions

1. One-body density distributions

In Fig. 5 we present the angular and radial (inset panel) helium density distributions around the dopant molecule. As above, the states that are invariant under reflexion with respect to z-inversion are marked with $\kappa=1$. The ground and low lying excited states belong to this class. As can be expected from the strong anisotropy of the $He-Cl_2$ potential (with a minimum at a T-shaped geometry) and small cluster sizes, the local angular density near the impurity is fairly structured and it clearly peaks around $\theta=90°$ (i.e., at a T-shaped configuration). We can see from the inset in Fig. 5 that the radial helium density distributions of these states become more diffuse and more biased toward larger R distances as the cluster size increases. On the other hand, the distributions associated with $N=1$ antisymmetric eigenstates, $\kappa=-1$, have two side peaks at $\theta\sim60°$ and 120° in the angular density and a peak shifted toward larger R distances in the radial density. The density near the Cl_2 polar regions is negligible even for the lowest-energy $\kappa=-1$ states. In fact, the spatial structure of the relevant $\kappa=-1$ orbitals resembles the two lateral rings around the dopant molecule as in Ref. 41. The larger the cluster size, the smaller the relative weights of $\kappa=-1$ orbitals in the FCI wave functions and therefore the above mentioned two-side-peaked structure for $N=1$ is less pronounced for $N=2$ and is not present at all for $N=3$ and 4. Also, the peak in the corresponding radial distributions becomes less shifted as the cluster size increases. As expected, the global picture emerging from the analysis of one-particle distributions is not different from that presented in previous studies of small ground-state $(^4He)_N-Cl_2$ clusters,[37,38,40,41,43] using pairwise-model potentials to characterize the global PES, and a semiempirical T-shaped PES to describe the $He-Cl_2$ interaction. Overall, due to the floppiness of the system, the distributions are rather broad (both radial and angular), with helium atoms located on a wide ring-shaped region around the dopant molecular axis.

2. Two-body density distributions

In Fig. 6, we plot the two-particle density distributions as a function of the relative angle, γ_{12}, for different cluster sizes. For $N=2$, it shows a maximum at $\gamma_{12}=180°$ and a shoulder at $\gamma_{12}\sim70°$. The global maximum at $\gamma_{12}=180°$ is present for larger cluster sizes while the shoulder becomes more pronounced for $N=3$ and transforms into a true maximum for $N=4$. In Fig. 7, we show the two-particle density distribution as a function of the interparticle distance, R_{12}, in the lowest-energy states of $(^3He)_N-Cl_2$ clusters for each

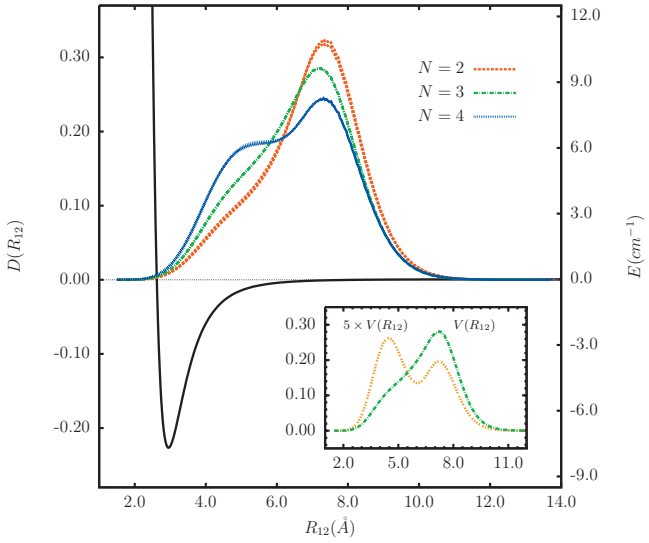

FIG. 7. Two-body density distributions as a function of the He–He distance, $D(R_{12})$, in the lowest-energy states of $(^3He)_N-Cl_2(B)$ clusters [using $\ell_{max}=8$ ($m_{max}=\ell_{max}$)]. The He–He interaction (in cm^{-1}) is also shown. The densities are normalized as $\int dR_{12}D(R_{12})=1$. Inset: comparison of the $D(R_{12})$ distribution obtained for $N=3$ with that calculated by using the V^{He-He} interaction multiplied by 5 (see text).

(N,S) manifold. We can notice that the density decay to zero just before the He–He interaction turns out to be repulsive. Interestingly, the pair probabilities are almost insensitive to the spin symmetry of the lowest-energy states. They have their maxima at about $R_{12}=2R_{eq}$, with R_{eq} being the He–Cl_2 equilibrium distance on the lowest one-particle states (see inset of Fig. 5). One can also distinguish a shoulder that becomes increasingly more pronounced as the cluster size increases, correlating with the feature at $\gamma_{12}=70°$ in the angular distributions from Fig. 6. Consequently, the shoulders are approximately located at $R_{12}=2R_{eq}\sin(\gamma_{12}/2)$. We believe that these secondary structures are responsible for the resulting negative average He–He interaction [see Fig. 1(b)]. In fact, as can be clearly seen from the pair density distribution for $N=4$ in Fig. 7, the secondary maximum enters into the minimum region of the He–He potential energy curve before overshooting its repulsive core. In order to render clearer the origin of the shoulder in the distributions, we performed additional calculations for $N=3$ with the He–He potential multiplied by 5 (inset of Fig. 7). If the shoulder at small R_{12} is caused by the attractive region of the He–He potential, it would be obviously more accentuated when a potential with a deeper He–He well depth is used whereas the relative weight of the maximum at large R_{12} should decrease. In fact, as can be clearly seen from the inset of Fig. 6, this is indeed the case. Interestingly, $D(R_{12})$ distributions peaking in the He–He well region and a global attractive He–He interaction (from -0.2 to -0.8 cm^{-1}) were already obtained by Barletta *et al.*[55] for $(^3He)_2$–SF_6 trimer using also a wave-function-based method. Indeed, the distributions reported in their work were peaked at a value ~4 Å which is not far from the location of the secondary feature for $N=4$ in Fig. 7, the average γ_{12} values (from 70° to 80°) being also close to the position of the shoulder or local maximum of $D(\cos\gamma_{12})$, see Fig. 6.

3. Global structures

From the analysis of one- and two-particle density distributions, in agreement with previous studies of the $(^4He_2)$–Cl_2 complex in its ground state,[37,38] it is predicted that the most stable structure for a $(^3He_2)$–Cl_2 cluster is planar with two He atoms located on the equatorial plane perpendicular to the Cl_2 molecular axis and at opposite ends of a vector of length $2R_{eq}$ passing through the dopant center of mass. However, the probability of a distorted tetrahedral structure, which correlates with the shoulder in the pair density distribution, is not negligible. The most stable structure for either ground-state $(^3He_3)$–Cl_2 or $(^3He_4)$–Cl_2 complexes, in which the ^{3}He atoms occupy unequivalent positions around the dopant within the equatorial ring plane, departs from the classical picture for $(^4He)_N$–Cl_2 and $(^4He)_N$–Br_2 complexes, the ^{4}He atoms being approximately equally spaced on the ring.[31,42] In contrast, the present results for $N=4$ fermions indicate the structural pairing of two ^{3}He atoms at opposite sides on a broad belt around the dopant, executing a sort of asymmetric umbrella motion. This pairing is a compromise between maximizing their mutual attraction, the one with Cl_2, and suppressing at the same time the hard-core repulsion. We remark that this structural pairing should not be confused with the spin-triplet pairing in liquid ^{3}He (see, e.g., Ref. 56). Overall, although the attractive region of the He-He potential is very shallow (about -7.5 cm^{-1}), its contribution increasingly affects the pair density distributions as the cluster grows in size. This could be easily understood by considering that, at least for small clusters, the contribution from the average attractive He–He potential interaction scales as $\binom{N}{2}$ whereas the contribution of the He-dopant potential interaction grows linearly with N.

Actually, we found that the per-pair averaged He–He attraction slightly (linearly) increases going from $N=2$ to $N=4$. This behavior is expected for larger N values (before filling the equatorial belt around the dopant). In principle, due to the screening and saturation effects, this per-pair attraction should scale as N^{-1} when the cluster size becomes very large. In fact, we are still very far from the bulk regime (see, e.g., Ref. 10) in which the evaporation energy is ~1.7 cm^{-1} (to be compared with about 8 cm^{-1} for the total energy per particle in our case).

D. Global analysis of the FCI wave-function structure

We found that a good representation of the FCI wave function is obtained by using cylindric coordinates and one-particle orbitals that can be expressed as

$$\psi_{v_\rho v_z m}(x,y,z)=\frac{1}{\sqrt{\rho}}o_{v_\rho v_z}(\rho,z)\frac{1}{\sqrt{2\pi}}e^{im\phi}.$$

The in-plane orbitals o are labeled using the quantum numbers v_ρ and v_z corresponding to vibrations along ρ and z, respectively.

We first consider the states symmetric with respect to z inversion, $\kappa=+1$, $(\Sigma_g,\Pi_u,\Delta_g,\cdots)$. They are formed from N-times occupied lowest in-plane orbital (0,0) and thus the (ρ,z) part will be denoted as $(0,0)^N$. Antisymmetric-in-z states, $\kappa=-1$, $(\Sigma_u,\Pi_g,\Delta_u,\cdots)$ correspond to one excited vibration along z and thus will be denoted as $(0,0)^{N-1}(0,1)$.

For a fixed (ρ,z) part, the angular wave function can be represented as a sum of angular factors $\Pi_{i=1}^{N}e^{im_i\phi_i}$ $(i=1,\ldots,N)$. Table III collects the results of such a model, for $N=2$–4, displaying individual terms as well as their weights in the total FCI wave function. Since the tails of the wave functions for $N=4$ are quite long, this analysis is much more complex and only two examples are given. In order to illustrate this analysis, we plot in Fig. 8 radial He–He pair density distributions, $D(R_{12})$, for ground and excited states of the complexes.

Assuming the He–He potential contribution to be a constant within a given (ρ,z) manifold (based on the very similar distributions from Fig. 8 and also on the rather close expectation values $\langle V^{He-He}\rangle$), the energy differences with respect to the lowest-energy state can be approximated as the difference in kinetic energy,

$$\Delta E_{est}=B_{eff}(\langle m_i^2\rangle_{exc}-\langle m_i^2\rangle_0),$$

where $\langle m_i^2\rangle=\Sigma_I w_I(\Sigma_i m_{I,i}^2)$, the "exc" and "0" subscripts denoting averages over the excited and lowest-energy states, respectively.

TABLE III. Decomposition of symmetric-in-z FCI wave functions in terms of configurations expressed as the products $\Pi_{i=1}^{N} e^{im_i\phi_i}$ $(i=1,\ldots,N)$. Weights of individual $(m_1,m_2,\cdots)$ configurations in the total wave functions, w, FCI energy differences with respect to the lowest-energy state within each N manifold, ΔE_{FCI}, and estimated values (see text), ΔE_{est}, are also indicated. Energies are in cm^{-1}.

State	$(m_1,m_2,\ldots)$	w	ΔE_{FCI}	ΔE_{est}
		$N=2$		
$^1\Sigma_g^+$	(0,0)	0.8	0	0
	(1,−1)	0.2		
$^3\Pi_u$	(1,0)	1.0	0.18	0.24
$^3\Sigma_g^-$	(1,−1)	1.0	0.47	0.64
$^1\Pi_u$	(1,0)	0.8	0.73	0.56
	(2,−1)	0.2		
$^1\Delta_g$	(1,1)	0.8	0.78	0.80
	(2,0)	0.2		
$^3\Delta_g$	(2,0)	1.0	1.32	1.44
		$N=3$		
$^4\Sigma_g^-$	(1,−1,0)	1.0	0	0
$^2\Pi_u$	(1,0,0)	0.5	0.17	0.20
	(1,−1,1)	0.33		
	(2,−1,0)	0.17		
$^2\Delta_g$	(1,1,0)	0.5	0.58	0.60
	(2,0,0)	0.25		
	(2,1,−1)	0.25		
$^4\Phi_u$	(2,1,0)	1.0	1.24	1.20
$^4\Delta_g$	(2,1,−1)	1.0	1.73	1.60
		$N=4$		
$^5\Delta_g$	(2,1,−1,0)	1.0	0	0
$^5\Pi_u$	(2,−2,1,0)	0.17	2.06	1.80
	(3,−3,1,0)	0.11		
	(3,2,−4,0)	0.07		
	(3,1,−2,−1)	0.03		

The one-particle rotational constant, B_{eff}, has been assumed to be 0.4 cm^{-1}. We can notice that this simple approximation provides accuracy for excitation energies within 2.5% for all cluster sizes. Focusing on $N=2$ and $N=3$ complex sizes, the discrepancies between estimated and exact values are less than 0.2 cm^{-1}, the larger ones (>0.1 cm^{-1}) obviously corresponding to states having different pair-density distributions as a function of the He–He distance (see Fig. 8).

For $N=4$, the underestimation of the energy difference between the $^5\Delta_g$ and $^5\Pi$ states is mostly due to the fact that the configurations displayed in Table III only account for 90% of the wave-function norm, other contributing configurations having very high m_i values (>4) and raising the ΔE_{est} value.

To demonstrate that these $m_i>4$ contributing configurations are relevant in determining the total energies and global structures for $N=4$, we performed additional calculations with a basis set characterized by $\ell_{\max}=9$ and $m_{\max}=4$. The results of these calculations are as follows: the energy of the ground state is underestimated by about 3.5 cm^{-1} (with respect to the $m_{\max}=\ell_{\max}$ case) and its angular pair density distribution is clearly peaked at $\gamma_{12}=90°$ and 180°. Also, we can notice that the energy underestimation is of the same order of magnitude as the total attractive contribution coming from six pairs of He atoms with an average He–He energy of −0.4 cm^{-1}.

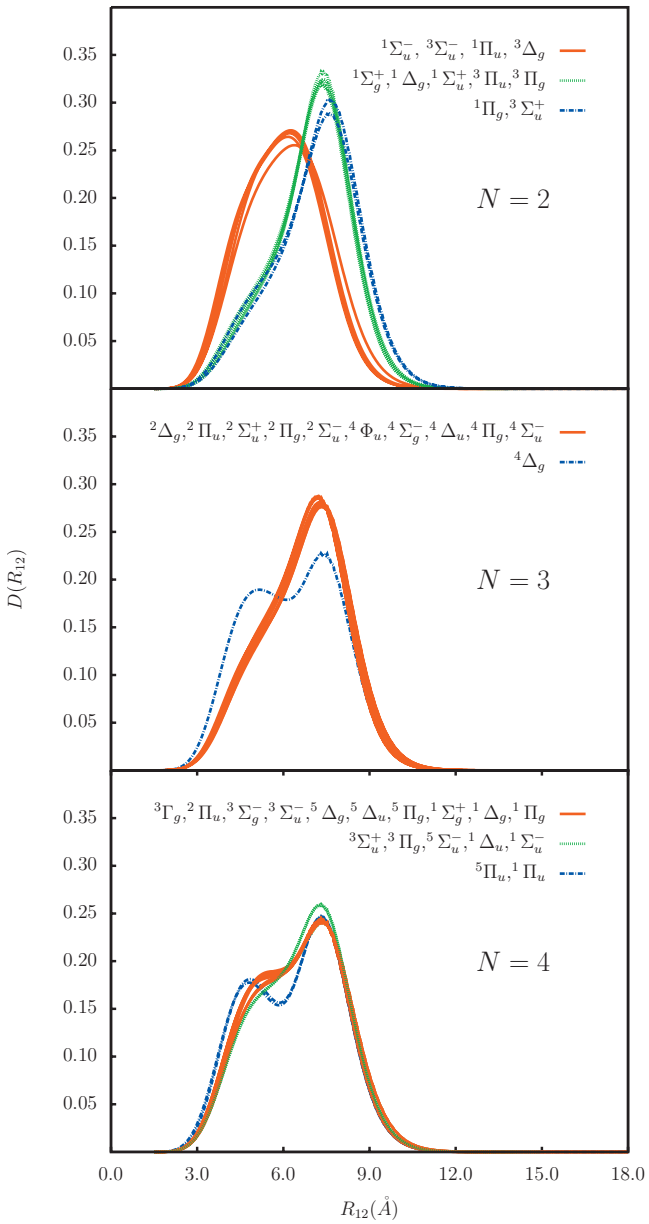

FIG. 8. Two-body density distributions as a function of the He–He distance, $D(R_{12})$, in the ground and excited states of $(^3\mathrm{He})_N$–$\mathrm{Cl}_2(B)$ clusters [using $\ell_{\max}=8$ $(m_{\max}=\ell_{\max})$].

The important conclusion from this wave-function analysis is that, in spite of very long (ℓ,m) tails, the in-plane (ρ,z) part of the wave function is essentially the same for all its components, being a product of well-defined single-particle orbitals. These orbitals are very close to the eigenfunctions of the two-dimensional in-plane one-particle operator. This suggests the use of an alternative basis for the full-CI approach; with just one or very few orbital (ρ,z) configurations, and a very large (m) basis, we hope to reproduce the results of the very big full-CI calculations presented in this work. The bottleneck of such a treatment is the much more involved evaluation of two-electron integrals. Work is in progress to implement such an approach. The use of this basis would allow a deeper analysis of the wave-function structure as well as the calculation of clusters with $N\geq 5$.

V. CONCLUDING REMARKS AND FUTURE PROSPECTS

The improvements of our optimized FCI implementation[32] to calculate solvent ground and excited-state energies and wave functions in small doped ^3He_N clusters have been described. The enhanced treatment has been applied to complexes containing $Cl_2(B)$ as dopant, using a highly anisotropic model T-shaped PES to describe the He-dopant interaction. The main conclusions of this study can be summarized as follows:

(1) The analysis of the convergence of total binding and average pair He–He interaction energies and relevant one- and two-body properties upon increasing the angular part of the basis set (expanded in spherical harmonics $Y_{m\ell}$) indicates that saturated functions ($m_{\max}=\ell_{\max}$) with very high one-particle angular momentum values are required to get reliable results, owing to the high-anisotropic degree of the $He-Cl_2$ interaction (high $\ell_{\max}$ values are necessary to represent localized-in-θ orbitals), and both the strongly repulsive core and weak attractive region of the He–He potential (high $m_{\max}$ values are essential to describe the long tails of the wave functions).

(2) Converged binding energies show a quasilinear dependence on the cluster size, in agreement to previous results for the $(^4He)_N-Cl_2$ clusters. The global analysis reveals that this particular behavior arises from the very delicate balance between the progressively more repulsive one-particle kinetic energy, due to the filling of rotational excited one-particle levels of the triatomic, and the increasingly more attractive contribution between $\binom{N}{2}$ pairs of ^{3}He atoms as N increases, the He-dopant interaction also scaling linearly with N.

(3) Pair radial density distributions display a shoulder when reaching the well region of the He–He potential, which falls off before overshooting its repulsive hard core. As a result, average $\langle V^{\text{He–He}}\rangle$ values per He–He pair are negative (from -0.2 to -0.5 cm^{-1}), showing a linear scaling with N. For $N=3$ and 4, ground and excited state pair density distributions are very similar.

(4) In agreement with previous results on $(^4He)_2-Cl_2$ complexes, the most stable structure is planar, with the Cl_2 center of mass in the middle of the two He atoms, which reside on an equatorial ring around the dopant. For $N=4$, the analysis of the density distributions suggests a favored structure with two ^{3}He "pairs" at opposite sides in a broad equatorial ring around the dopant molecule, departing from the global ground-state structure of N ^{4}He atoms equally spaced around the dopant within the equatorial plane in $(^4He)_N-Cl_2$ complexes.[31] As found in the $^3He_2-SF_6$ trimer,[55] the attractive part of the He–He potential is also relevant to determine the more favored spatial arrangements in these clusters.

(5) The quantitative analysis of the configurational makeup of FCI wave functions strongly indicates the robustness of its decomposition in terms of a single configuration, depending on the cylindrical coordinates $\{\rho_i,z_i\}$, and of a sum over basis-set configurations expressed as the products: $\Pi_{i=1}^{N}e^{im_i\phi_i}$ $(i=1,\ldots,N)$.

It is also worth recalling that the conclusions reached in our previous works using relatively small basis sets[32,35] (stressing the efficiency of the JD iterative solver in hard-core interaction problems, the high degree of degeneracy attained by the lowest-energy spin multiplets, and the robustness of the nuclear orbital approach) are still valid. Considering the high degeneracy of energy levels, we gained further insight by proving that the lowest-energy states at each (N,S) manifold have almost identical pair density distributions, the effective He–He interaction being thus quite similar. In a forthcoming work,[54] we will analyze the influence of using either a semiempirical model T-shaped $He-Cl_2(X)$ potential or an *ab initio* one with minima at T-shaped and linear configurations, visualizing how energetic and structural aspects of the helium environment are reflected in the rovibrational spectra of the dopant.

Obvious directions for future work include the extension of the FCI treatment to study small doped ^{4}He and mixed $^4He/^3He$ clusters and to incorporate into the calculations the nonadiabatic interaction induced by the overall dopant-molecule rotation.[57] In addition, the present study provided the hints for devising a more cost-effective FCI implementation through the expansion of the basis set in terms of optimized two-dimensional (ρ,z) functions (using $N=1$ eigenfunctions) and the standard $e^{-im\phi}$ ones. It is also worth noting that, apart from the lowest-energy highest spin states, the high multireference character of the wave function together with an increasing contribution of "dynamical correlation" accounting for its short-range structure as the cluster grows in size, prevents from using less expensive high-level *ab initio* electronic structure methods without sacrificing the hard-core region of the He–He potential. Taking advantage of the single-reference character of the lowest-energy highest spin-states wave functions, however, it seems affordable to apply coupled-cluster methods[58,59] to calculate them. A compromise between precision and cost efficiency could be reached in the spirit of density-functional-based embedding approaches first proposed by Wesolowski and Washell[60] in the framework of electronic structure problems. In this regard, the recent work by Barranco and co-workers[10,61] on mixed He nanodroplets by their developed DFT approach, which is tailored to match the bulk He regime, is particularly reassuring. Work along these lines is currently in progress.

Finally, besides accurately describing the ground and excited states of small doped helium clusters, benchmark FCI nuclear orbital calculations may help shed light on the definition of the nodal trial function in fixed-node diffusion Monte Carlo simulations,[62] which is an active area of research in the study of pure and doped He clusters or, in general, in the field of weakly bound complexes.[20] Alternatively, the FCI method could serve to test novel Monte Carlo approaches for ^{3}He clusters without *a priori* information of the nodal structure of the wave function as the newly one proposed in the framework of electronic structure problems.[63]

ACKNOWLEDGMENTS

This work has been partially supported by the CSIC-CAM, CICYT, and MICINN-CSIC Spanish Grants Nos. CCG08-CSIC/ESP-3680, FIS2007-62006, and 2007501004. The Centro de Supercomputación de Galicia (CESGA) and the Centro de Supercomputación y Visualización de Madrid (Ref. No. AB01101001) are acknowledged for allocation of computer time. We would like to thank Professor C. Valdemoro, Professor M. Barranco, Dr. M. I. Hernández, Dr. A. García-Vela, and N. Aguirre for very fruitful discussions.

APPENDIX A: CALCULATION OF TWO-PARTICLE PROPERTIES

The calculation of $\langle \hat{\mathbf{L}}^2 \rangle$ is based on the resolution of identity (RI):

$$\langle 0|\hat{A}\hat{B}|0\rangle = \sum_I \langle 0|\hat{A}|I\rangle\langle I|\hat{B}|0\rangle, \tag{A1}$$

where $\hat{A}=\hat{B}=\hat{L}$. In principle, this relation is exact when a complete, infinite, expansion is used. For any finite set, like FCI, this RI is only an approximation. However, if one-particle basis is closed under the action of the operators $\hat{A}$ and $\hat{B}$, the corresponding multiconfigurational basis $\{|I\rangle\}$ will also be closed, and then the finite sum in RI will give the exact answer. This is the case for the angular momentum operator $\hat{L}$ and one-electron basis of the type $R_n(r)Y_{lm}(\theta,\phi)$, provided that $m_{\max}=l_{\max}$.

The implementation of RI can be done efficiently. If we write the reference state as $|0\rangle=\Sigma_I C_I^0|I\rangle$, we can define, using RI,

$$|\hat{B}0\rangle = \sum_I |I\rangle\langle I|\hat{B}|0\rangle \equiv \sum_I C_I^{\hat{B}0}|I\rangle. \tag{A2}$$

The evaluation of the coefficients $C_I^{\hat{B}0}$ is equivalent to the action of a one-particle operator and can be implemented very efficiently using our FCI techniques. The needed time/memory is negligible compared to the FCI calculation itself. Once these coefficients are evaluated and stored, we can easily calculate all required matrix elements (e.g., $\langle 0|\hat{B}|0\rangle = \Sigma_I C_I^{0*} C_I^{\hat{B}0}$ and $\langle 0|\hat{A}\hat{B}|0\rangle = \Sigma_I C_I^{\hat{A}^\dagger 0*} C_I^{\hat{B}0}$).

APPENDIX B: METHOD FOR ANGULAR MOMENTUM PROJECTION

Since our implementation includes an algorithm to apply the operator $\hat{\mathbf{L}}$ to the FCI wave function (provided that $m_{\max}=j_{\max}$), its further projection to a wave function with a given eigenvalue of $\hat{\mathbf{L}}^2$ [equal to $L(L+1)$] is straightforward, using standard discrete operator projector:

$$\hat{P}_L = \prod_{\lambda \neq L} \frac{\hat{\mathbf{L}}^2 - \lambda(\lambda+1)}{L(L+1)-\lambda(\lambda+1)}, \tag{B1}$$

where the product is taken over all possible eigenvalues of $\hat{\mathbf{L}}^2$ different from $L(L+1)$.

Here, in order to develop a stable numerical implementation, some attention should be paid to the order in which different λ projections are applied in Eq. (B1). Our algorithm recurrently checks for the λ component having largest weight in the residual wave function and projects it out.

APPENDIX C: EVALUATION OF PAIR DENSITY DISTRIBUTIONS

In order to evaluate the angular pair density distributions, $D(\cos\gamma_{12})$, we assume an expansion in Legendre polynomials,[37]

$$D(\cos\gamma_{12}) = \sum_\Lambda d_\Lambda P_\Lambda(\cos\gamma_{12}), \tag{C1}$$

where

$$d_\Lambda = \frac{2\Lambda+1}{2} \sum_{n_1\ell_1 m_1} \sum_{n_2\ell_2 m_2} \sum_{n_1'\ell_1' m_1'} \sum_{n_2'\ell_2' m_2'} \times \Gamma_{(n_1\ell_1 m_1),(n_2\ell_2 m_2);(n_1'\ell_1' m_1'),(n_2'\ell_2' m_2')} \times \langle \chi^{(n_1\ell_1 m_1)}\chi^{(n_2\ell_2 m_2)}|P_\Lambda(\cos\gamma_{12})|\chi^{(n_1'\ell_1' m_1')}\chi^{(n_2'\ell_2' m_2')}\rangle, \tag{C2}$$

$\Gamma_{ij;kl}$ being the standard second-order reduced density matrix. Taking into account the "spherical harmonic addition" theorem and evaluating the integral over three spherical harmonics,[64] the $\langle\cdots\rangle$ integral from Eq. (C2) can be expressed as

$$\begin{aligned}
&\langle \chi^{(n_1\ell_1 m_1)}\chi^{(n_2\ell_2 m_2)}|P_\Lambda(\cos\gamma_{12})|\chi^{(n_1'\ell_1' m_1')}\chi^{(n_2'\ell_2' m_2')}\rangle \\
&= \delta_{n_1,n_1'}\delta_{n_2,n_2'}(-1)^{m_1-m_1'}\delta_{m_1+m_2,m_1'+m_2'} \\
&\quad \times \sqrt{(2\ell_1+1)(2\ell_2+1)(2\ell_1'+1)(2\ell_2'+1)} \begin{pmatrix} \ell_1 & \Lambda & \ell_1' \\ 0 & 0 & 0 \end{pmatrix} \\
&\quad \times \begin{pmatrix} \ell_1 & \Lambda & \ell_1' \\ -m_1 & m_1-m_1' & m_1' \end{pmatrix} \begin{pmatrix} \ell_2 & \Lambda & \ell_2' \\ 0 & 0 & 0 \end{pmatrix} \\
&\quad \times \begin{pmatrix} \ell_2 & \Lambda & \ell_2' \\ -m_2 & m_2-m_2' & m_2' \end{pmatrix}.
\end{aligned} \tag{C3}$$

Evaluation of the radial pair density distributions, $D(R_{12})$, is performed by first fixing R_1 and R_2 values and getting $d_\Lambda(R_1,R_2)$ coefficients. To calculate these expansion coefficients, it is only important to realize that the product $\delta_{n_1,n_1'}\delta_{n_2,n_2'}$ from Eq. (C3) should be replaced by $\Sigma_{n_1,n_1',n_2,n_2'}(F^2_{n_1}(R_1)F^2_{n_1'}(R_1)F^2_{n_2}(R_2)F^2_{n_2'}(R_2))$. Hereafter, using the relation $\cos\gamma_{12}=(R_1^2+R_2^2-R_{12}^2)/(2R_1R_2)$ and the Jacobian of the transformation from $(R_1,R_2,\gamma)\rightarrow(R_1,R_2,R_{12})$, the distribution on R_{12} is given by

$$D(R_{12}) = \sum_\Lambda \left(\int\int dR_1 dR_2 \frac{R_{12}}{R_1R_2} d_\Lambda(R_1,R_2) \right) P_\Lambda(\cos\gamma_{12}), \tag{C4}$$

where the integration $\int\int dR_1 dR_2(\cdots)$ has been performed by employing a Gauss–Legendre quadrature procedure.

[1] S. Goyal, D. L. Schutt, and G. Scoles, Phys. Rev. Lett. **69**, 933 (1992).
[2] J. P. Toennies and A. F. Vilesov, Angew. Chem., Int. Ed. **43**, 2622 (2004).

[3] S. Grebenev, J. P. Toennies, and A. F. Vilesov, Science **279**, 2083 (1998).
[4] S. Grebenev, M. Hartmann, M. Havenith, B. Sartakov, J. P. Toennies, and A. F. Vilesov, J. Chem. Phys. **112**, 4485 (2000).
[5] J. Tang, Y. Xu, A. R. W. McKellar, and W. Jäger, Science **297**, 2030 (2002).
[6] J. Tang, A. R. W. McKellar, F. Mezzacapo, and S. Moroni, Phys. Rev. Lett. **92**, 145503 (2004).
[7] A. R. W. McKellar, Y. Xu, and W. Jäger, Phys. Rev. Lett. **97**, 183401 (2006).
[8] Y. Xu, N. Blinov, W. Jäger, and P. N. Roy, J. Chem. Phys. **124**, 081101 (2006).
[9] L. A. Surin, A. V. Potapov, B. S. Dumesh, S. Schlemmer, Y. Xu, P. L. Raston, and W. Jäger, Phys. Rev. Lett. **101**, 233401 (2008).
[10] M. Barranco, R. Guardiola, S. Hernández, R. Mayol, J. Navarro, and M. Pí, J. Low Temp. Phys. **142**, 1 (2006).
[11] B. J. Garrison, W. A. Lester, Jr., and H. F. Schaefer III, J. Chem. Phys. **63**, 1449 (1975).
[12] S. Moroni, N. Blinov, and P. N. Roy, J. Chem. Phys. **121**, 3577 (2004).
[13] F. Paesani, A. Viel, F. A. Gianturco, and K. B. Whaley, Phys. Rev. Lett. **90**, 073401 (2003).
[14] C. Di Paola, F. A. Gianturco, D. López-Durán, M. P. de Lara-Castells, G. Delgado-Barrio, P. Villarreal, and J. Jellinek, ChemPhysChem **6**, 1348 (2005).
[15] K. Kwon, F. Paesani, and K. B. Whaley, Phys. Rev. B **74**, 174522 (2006).
[16] S. Miura, J. Chem. Phys. **126**, 114308 (2007).
[17] Z. Li, L. Wang, H. Ran, D. Xie, N. Blinov, P. N. Roy, and H. Guo, J. Chem. Phys. **128**, 224513 (2008).
[18] S. Baroni and S. Moroni, in *Quantum Monte Carlo Methods in Physics and Chemistry*, NATO Series, Mathematical and Physical Sciences Vol. 525, edited by P. Nightingale and C. J. Umrigar (Kluwer Academic, Boston, 1999).
[19] P. Cazzato, S. Paolini, S. Moroni, and S. Baroni, J. Chem. Phys. **120**, 9071 (2004).
[20] A. B. McCoy, Int. Rev. Phys. Chem. **25**, 77 (2006).
[21] E. Sola, J. Casulleras, and J. Boronat, Phys. Rev. B **73**, 092515 (2006).
[22] P. Jungwirth and A. Krylov, J. Chem. Phys. **115**, 10214 (2001).
[23] M. P. de Lara-Castells, R. Prosmiti, D. López-Durán, G. Delgado-Barrio, P. Villarreal, F. A. Gianturco, and J. Jellinek, Int. J. Quantum Chem. **107**, 2902 (2007).
[24] O. Roncero, R. Pérez-Tudela, M. P. de Lara-Castells, R. Prosmiti, G. Delgado-Barrio, and P. Villarreal, Int. J. Quantum Chem. **107**, 2756 (2007).
[25] O. Roncero, M. P. de Lara-Castells, G. Delgado-Barrio, P. Villarreal, T. Stoecklin, A. Voronin, and J. C. Rayez, J. Chem. Phys. **128**, 164313 (2008).
[26] D. López-Durán, M. P. de Lara-Castells, G. Delgado-Barrio, P. Villarreal, C. Di Paola, F. A. Gianturco, and J. Jellinek, Phys. Rev. Lett. **93**, 053401 (2004).
[27] D. López-Durán, M. P. de Lara-Castells, G. Delgado-Barrio, P. Villarreal, C. Di Paola, F. A. Gianturco, and J. Jellinek, J. Chem. Phys. **121**, 2975 (2004).
[28] M. P. de Lara-Castells, D. López-Durán, G. Delgado-Barrio, P. Villarreal, C. Di Paola, F. A. Gianturco, and J. Jellinek, Phys. Rev. A **71**, 033203 (2005).
[29] M. P. de Lara-Castells, R. Prosmiti, D. López-Durán, G. Delgado-Barrio, P. Villarreal, F. A. Gianturco, and J. Jellinek, Phys. Rev. A **74**, 053201 (2006).
[30] P. Villarreal, M. P. de Lara-Castells, R. Prosmiti, G. Delgado-Barrio, C. Di Paola, F. A. Gianturco, and J. Jellinek, Phys. Scr. **76**, C96 (2007).
[31] P. M. Felker, J. Chem. Phys. **125**, 184313 (2006).
[32] M. P. de Lara-Castells, G. Delgado-Barrio, P. Villarreal, and A. O. Mitrushchenkov, J. Chem. Phys. **125**, 221101 (2006).
[33] E. R. Davidson, J. Comput. Phys. **17**, 87 (1975).
[34] G. L. G. Sleijpen and H. A. Van der Vorst, SIAM J. Matrix Anal. Appl. **17**, 401 (1996).
[35] M. P. de Lara-Castells, A. O. Mitrushchenkov, G. Delgado-Barrio, and P. Villarreal, Few-Body Syst. **45**, 233 (2009).
[36] W. D. Sands, C. R. Bieler, and K. C. Janda, J. Chem. Phys. **95**, 729 (1991).
[37] P. Villarreal, O. Roncero, and G. Delgado-Barrio, J. Chem. Phys. **101**, 2217 (1994).
[38] M. I. Hernández, N. Halberstadt, and W. D. Sands, J. Chem. Phys. **113**, 7252 (2000).
[39] A. García-Vela, J. Chem. Phys. **122**, 014312 (2005).
[40] M. A. McMahon and K. B. Whaley, J. Chem. Phys. **103**, 2561 (1995).
[41] T. Takayanagi, M. Shiga, and T. Taketsugu, J. Theor. Comput. Chem. **4**, 197 (2005).
[42] C. García-Rizo, M. I. Hernández, A. García-Vela, P. Villarreal, and G. Delgado-Barrio, J. Mol. Struct. (Theochem). **493**, 125 (1999).
[43] Z. Bačić, M. Kennedy-Mandziuk, J. M. Moskowitz, and K. E. Schmidt, J. Chem. Phys. **97**, 6472 (1992).
[44] A. Valdés, R. Prosmiti, P. Villarreal, and G. Delgado-Barrio, J. Chem. Phys. **125**, 014313 (2006).
[45] A. O. Mitrushenkov, Chem. Phys. Lett. **217**, 559 (1994).
[46] S. Rettrup, Chem. Phys. Lett. **47**, 59 (1977).
[47] MOLPRO, version 2006.1, a package of *ab initio* programs designed by H.-J. Werner and P. J. Knowles, see http://www.molpro.net.
[48] H. J. Werner and P. J. Knowles, J. Chem. Phys. **89**, 5803 (1988).
[49] P. J. Knowles and H. J. Werner, Chem. Phys. Lett. **145**, 514 (1988).
[50] R. Barrett, M. Berry, T. Chan, J. Demmel, J. Donato, J. Dongarra, V. Eijkhout, R. Pozo, C. Romine, and H. A. Van der Vorst, *Templates for the Solution of Linear Systems: Building Blocks for Iterative Methods* (SIAM, Philadelphia, 1994).
[51] R. A. Aziz and M. J. Slaman, J. Chem. Phys. **94**, 8047 (1991).
[52] A. García-Vela, J. Chem. Phys. **119**, 5583 (2003).
[53] J. Williams, A. Rohrbacher, J. Seong, N. Marianayagam, K. C. Janda, R. Burcl, M. M. Szcześniak, G. Chalasiński, S. M. Cybulski, and N. Halberstadt, J. Chem. Phys. **111**, 997 (1999).
[54] M. P. de Lara-Castells, A. O. Mitrushchenkov, G. Delgado-Barrio, and P. Villarreal (unpublished).
[55] P. Barletta, A. Fabrocini, A. Kievsky, J. Navarro, and A. Polls, Phys. Rev. A **68**, 053205 (2003).
[56] A. Leggett, Rev. Mod. Phys. **47**, 331 (1975).
[57] M. P. de Lara-Castells, A. Mitrushenkov, P. Palmieri, F. L. Quére, C. Leonard, and P. Rosmus, Mol. Phys. **98**, 1713 (2000).
[58] H. J. Klummer, in *Recent Progress in Many-Body Theories*, edited by R. F. Bishop, T. Brandes, K. Gernoth, N. Walet, and Y. Xian (World Scientific, Singapore, 2002), p. 334.
[59] J. Cízek and J. Paldus, Int. J. Quantum Chem. **5**, 359 (1971).
[60] T. Wesolowski and A. Washell, J. Phys. Chem. **97**, 8050 (1993).
[61] O. Bünermann, M. Dvorak, F. Stiekemeir, A. Hernando, R. Mayol, M. Pi, M., Barranco, and F. Ancilotto, Phys. Rev. B **79**, 214511 (2009).
[62] R. Guardiola, J. Navarro, D. Mateo, and M. Barranco, J. Chem. Phys. **131**, 174110 (2009).
[63] G. Booth, A. Thom, and A. Alavi, J. Chem. Phys. **131**, 054106 (2009).
[64] R. Zare, *Angular Momentum* (Wiley, New York, 1988).